CORA Cork Open Research Archive
Cartlann Taighde Oscailte Chorcaí

Title	Semiconductor nanostructures for antireflection coatings, transparent contacts, junctionless thermoelectrics and Li-ion batteries
Authors	Glynn, Colm;Osiak, Michal J.;McSweeney, William;Lotty, Olan;Jones, Kim;Geaney, Hugh;Quiroga-Gonzalez, Enrique;Holmes, Justin D.;O'Dwyer, Colm
Publication date	2013-10
Original Citation	Glynn, C., Osiak, M., McSweeney, W., Lotty, O., Jones, K., Geaney, H., Quiroga-González, E., Holmes, J. D. and O'Dwyer, C. (2013) '(Invited) Semiconductor Nanostructures for Antireflection Coatings, Transparent Contacts, Junctionless Thermoelectrics and Li-Ion Batteries', ECS Transactions, 53(6), pp. 25-44. doi: 10.1149/05306.0025ecst
Type of publication	Article (peer-reviewed)
Link to publisher's version	10.1149/05306.0025ecst
Rights	© 2013 ECS - The Electrochemical Society
Download date	2025-01-12 21:58:08
Item downloaded from	http://ecst.ecsdl.org/content/53/6/25.abstract

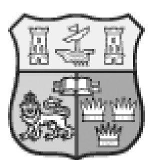

UCC
University College Cork, Ireland
Coláiste na hOllscoile Corcaigh

Semiconductor Nanostructures for Antireflection Coatings, Transparent Contacts, Junctionless Thermoelectrics and Li-ion Batteries

C. Glynn[1,2], M. Osiak[1], W. McSweeney[1,3], O. Lotty[5], K. Jones[3], H. Geaney[1,2], E. Quiroga-González[6], J. D. Holmes[2,5,7], and C. O'Dwyer[1,2,4]

[1] *Department of Chemistry, University College Cork, Cork, Ireland*
[2] *Micro- and Nanoelectronics Centre, Tyndall National Institute, Lee Maltings, Cork, Ireland*
[3] *Department of Physics & Energy, University of Limerick, Limerick, Ireland*
[4] *Materials and Surface Science Institute, University of Limerick, Limerick, Ireland*
[5] *Materials Chemistry and Analysis Group, Department of Chemistry University College Cork, Cork, Ireland*
[6] *Institute for Materials Science, Christian-Albrechts Universität, Kiel, Germany*
[7] *Centre for Research on Adaptive Nanostructures and Nanodevices (CRANN), Trinity College Dublin, Dublin 2, Ireland*

Porous semiconductors structured top-down by electrochemical means, and from bottom-up growth of arrays and arrangements of nanoscale structures, are shown to be amenable to a range of useful thermal, optical, electrical and electrochemical properties. This paper summarises recent investigations of the electrochemical, electrical, optical, thermal and structural properties of porous semiconductors such as Si, In_2O_3, SnO_2 and ITO, and dispersions, arrays and arrangements of nanoscale structures of each of these materials. We summarize the property-inspired application of such structurally engineered arrangements and morphologies of these materials for antireflection coatings, broadband absorbers, transparent contacts to LEDs that improve transmission, electrical contact and external quantum efficiency. Additionally the possibility of thermoelectric performance through structure-mediated variation in thermal resistance and phonon scattering without a p-n junction is shown through phonon engineering in roughened nanowires. Lastly, we show that bulk crystals and nanowires of p- and n-type doped Si are promising for use as anodes in Li-ion batteries.

Introduction

Porous semiconductors continue to receive considerable attention because of functionality afforded by random or ordered structuring on the nano or mesoscale. For instance, a wide range of mono- and compound semiconductors can be rendered porous through electroless or electrochemical etching (1-26), and such top down approaches allow a high degree of control over porosity formation. Additionally, the resulting skeleton formed through these means allows the possibility for arrays or arrangements of nanostructured materials such as nanowires (NWs), mesoporous materials, nanorods, photonic crystals and many other structural forms. When the

sizes of the remaining semiconductors is reduced, photonic and phononic confinements effects can allow for rich optical and thermal effects not possible in the bulk materials. Additionally, porous materials can often alleviate structural changes when applied as electrodes in Li-ion batteries and other phase change or structure converting processes. Silicon has maintained a strong fundamental and applied research value, and recently has become one of the most significant materials, when structured on the nanoscale, for Li-ion battery anodes (27-29) and in thermoelectric materials evaluation (30-32).

Transparent conducting oxides are also of prime importance for electronic and photonic devices. Their major limitation is the trade-off between their conductivity and transparency (33), which can be overcome to some extent through controlled top-down or bottom up porosity formation, or effective porosity formation through nanostructured growth methods. In developing techniques to fabricate homogeneous one-dimensional (1D) nanostructures, researchers have sought to control shape, aspect ratio and crystalline arrangement (34-35), and recent improvements in synthetic methods (36-38) have led to the direct integration of functional nanostructures into nanoscale devices. Indium tin oxide (ITO) (39,40) is the most important transparent conducting oxide and is therefore used in a wide range of applications. However, to date it has enjoyed only limited success as an ohmic contact for light-emitting devices (LEDs) due to high resistivities and an unacceptable trade-off between electrical and optical characteristics. Moreover, the limited availability of materials with suitable refractive indices has prevented the implementation of optical components with high performance. Hence, the possibility of forming complex, multilevel branched structures (41) with optimized optical properties in a single-step, bottom-up growth regime would be a significant advance given their compatibility with optoelectronic device architectures. The development of high mobility oxides, or dispersion of metallic NWs that offer percolating conductivity and porosity to mimic a transparent conductive thin film, are important for charge storage devices such as batteries and pseudocapacitors, planar and flexible electronic and photonic devices.

Rechargeable batteries have been critical for enabling portable consumer electronics and are beginning to be used in electric vehicles. They are also becoming an attractive option for large-scale stationary energy storage (42-47). For mobile applications, high energy (per weight and volume) is the most important parameter since it determines the usage time per charge. For stationary applications, cost is the most important design parameter, and high energy batteries could help reduce the cost per unit of stored energy (48,49).

The continued development of porous structures for these reasons also has translational application to thermoelectrics and paradigms for energy harvesting from waste heat on the nanoscale in electronic devices, particularly LEDs and other high power devices, and the structuring of the porous semiconductors can tunable alter the thermal resistance of materials, allowing thermoelectric voltage generation without requiring a p-n junction. These types of materials and strategies to induced controlled porosity for a variety of functions are summarized for a series of common electronic and transparent oxide-type semiconductors.

Experimental

Molecular beam epitaxial growth of In_2O_3, SnO_2 and ITO nanodots and NWs

All surfaces were cleaned using a standard RCA process where the sample was immersed in a H_2O_2:NH_4OH:H_2O (1:1:1) solution at 80°C for 30 min. After rinsing in deionised water, a second treatment was performed in a H_2O_2:HCl:H_2O (1:1:5) solution with subsequent rinsing in deionized water. Through this process metallic and organic contamination is removed. In the latter step, the surface is oxidized so that a thin (~7 nm) and clean SiO_2 layer forms at the surface. Dipping the sample in HF shortly before introducing it into the evaporator removes the oxide layer and passivates the surface with hydrogen. For evaporation of the In and Sn sources, a home-built MBE high vacuum chamber with two distinct effusion cells for In and Sn together with an electron-beam evaporator, was designed in cooperation with MBE-Komponenten GmbH, Germany, with calibrated growth rates. During NW growth the sample surface was annealed at temperatures in the range 300°-650 °C. The In:Sn (90:10) was evaporated at growth rates in the range 0.02-0.2 nm s^{-1} up to maximum temperature for In and Sn of T_{In} = 835 °C, T_{Sn} = 1000 °C, respectively.

For In_2O_3 and SnO_2 nanodot dispersions, uniform layers of In and Sn metal were grown on respective substrates by depositing at a rate of 0.1 Å s^{-1} at a substrate temperature of 400 °C, with precise control over the nominal thickness, which was separately calibrated using a quartz crystal monitor. The nanodots then results from dewetting and oxidative crystallization.

Growth of Si/SiGe multi-quantum well devices

The n-i-p^+ Si/SiGe multi quantum well (MQW) structures were grown by molecular beam epitaxy (MBE). On an 80 nm undoped Si buffer grown at 700 °C on Si(001), a 15-period Si/$Si_{0.77}Ge_{0.23}$ (4.1 nm/3.9 nm) quantum well structure was deposited at 625 °C. The entire structure was capped with 42 nm B-doped (5×10^{18} cm^{-3}) Si to saturate SiGe dangling bonds. After an additional 10 nm Si top layer grown at 625 °C, a capping layer of 30 nm p^+-Si (p-doped) was grown at 700 °C. The back contact was a Ti (50 nm diffusion barrier)/Pt (50 nm)/Au (100 nm) multilayer ohmic contact. Several structures were top-contacted with a Ni/Cr bilayer deposited by sputtering.

Metal-assisted electroless etching of Si NW layers

Layers of p-type and n-type Si NWs, were fabricated by metal-assisted chemical (MAC) etching of 200 mm diameter lightly p-doped silicon (100) wafers (680 µm thickness) and highly doped n-type wafers, both with a native oxide layer (~2-5 nm thick). Substrates were immersed for two hours in a heated solution of 10% HF containing 0.04 M $AgNO_3$ and maintained at 50 °C using a thermostated water bath. Upon removal from the etching bath, samples were washed copiously with deionised water and then treated with concentrated nitric acid to remove unwanted silver deposition. The length of the NWs was controlled by the etching time and etchant concentration leaving a uniform, effective porous silicon layer. The remaining skeleton formed a vertical array of NWs ranging from 80 – 200 nm in diameter.

Optical, PL/EL and Raman spectroscopy measurements

Optical excitation came from a 6 W Argon ion (Ar^+) laser (Spectra Physics *Stabilite* 2017) operating at 514.5 nm. Luminescence was collected through a SPEX 1680 double monochromator into a cooled North Coast EO-817L Ge detector. For

photoluminescence (PL) and electroluminescence (EL) measurements, a pulsed excitation optical signal with a fixed frequency of 590 Hz and an electrical signal pulsed at 570 Hz, respectively, were used and modulated by a mechanical chopper. The output from the chopper was fed through a lock-in amplifier measuring the output signal of the Ge detector sensitive in a spectral range 0.8-1.7 μm. Reflectance measurements were carried out in a Bruker FT-IR spectrometer IFS66/V. Different configurations of beam splitters, detectors and sources were used to cover the spectral range from a far infrared (10 cm^{-1}) to near infrared and visible ranges. For angular resolved measurements, a NIR512 Ocean Optics spectrometer was used as a detector in a home-built reflectance/transmittance setup.

Comparative photo- and electroluminescence (PL/EL) measurements were performed on Si/SiGe MQW LEDs grown by MBE. To compare the optical transmission, an ITO NW layer and a 30 nm NiCr metal contact were deposited on two separate samples on the same substrate. As a reference, the photoluminescence spectrum of an uncoated MQW structure was recorded under identical conditions.

Raman spectroscopy was conducted using a Dilor XY Labram spectrometer equipped with an Olympus BX40 confocal microscope and Renishaw InVia Raman spectrometer using a RenCam CCD camera. Excitation was provided by 514 nm ArHe 10 mW green laser with a maximum of 0.512 mW incident power. The spectra were collected with a Peltier cooled CCD detector. The incident power of the laser was adjusted using calibrated filters.

Structural, compositional and morphological characterization

All materials and samples were analysed using scanning and transmission electron microscopy (SEM/TEM). SEM was performed using both Hitachi S4800 and SU70 instruments equipped with an Oxford-50 mm^2 X-Max detector for energy dispersive X-ray analysis. TEM analysis was conducted with a JEOL JEM-2100F field emission microscope operating at 200 kV, equipped with a Gatan Ultrascan CCD camera and EDAX Genesis EDS detector for atomic resolution crystal structure and composition examination. For ultra-high resolution morphology, STEM and high angle annular dark field (HAADF) couple with electron diffraction was performed. X-ray diffraction (XRD) spectra were made using Cu Kα radiation with a Philips PanAlytical diffractometer in Bragg-Bretano geometry.

X-ray photoelectron spectroscopy was acquired using a Kratos Axis 165 monochromatized X-ray photoelectron spectrometer equipped with a dual anode (Mg/Al) source. Survey spectra were captured at as pass energy of 100 eV, step size of 1 eV, and dwell time of 50 ms. The core level spectra were an average of 10 scans captured at a PE of 25 eV, step size of 0.05 eV, and dwell time of 100 ms. The spectra were corrected for charge shift to the C 1s line at a binding energy of 284.9 eV. A Shirley background correction was employed, and the peaks were fitted to Voigt profiles.

Electrochemical analysis in Li-ion battery cells

Cyclic voltammetry and galvanostatic measurements were carried out using either 3-electrode cells or 2-electrode coin cells using a Multi Autolab 101 potentiostat and a BioLogic VSP potentio/galvanostat. All potentials, unless otherwise stated, are relative to Li^+/Li. Custom built Swagelok-type cells, split coin cells were used with counter and active material electrodes separated by a polypropylene or glass wool separators soaked in 1 mol dm^{-3} solution of $LiPF_6$ in EC:DMC at a 50:50 v/v ratio.

The electrodes were cycled at a scan rate of 0.5 mV/s in cyclic voltammetric measurements. Afterwards, electrodes were carefully washed in acetonitrile and a 10^{-4} mol dm^{-3} solution of acetic acid to remove the electrolyte residue.

Results and Discussion

Antireflective transparent coatings, and tunable or broadband absorption layers

Transparent conducting oxide NWs were grown using a unique self-seeding process during MBE deposition that results in defect-free branched NW layers whose composition can be tuned as well as the graded porosity and thus refractive index. For a given angle, the internal optical scattering (a balance of Rayleigh scattering, material absorption and effective medium graded index effects) allows a tunable absorption depending on the NW size, distribution, branching and overall photonic morphology. An example of the NW layer is shown below in Fig. 1a.

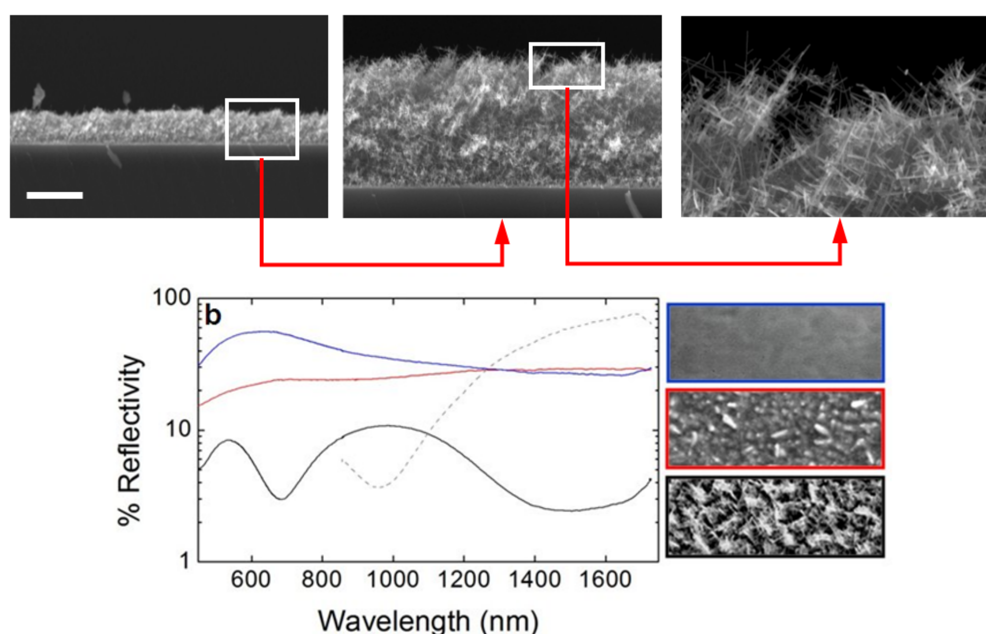

Figure 1. (a) A typical ITO NW layer grown on Si(100). The layer comprises a high density of branched NWs, which grow from a near compact contact layer to Si, followed by increased porosity from lower density growth away from the substrate. (b) Reflectance spectra for (——) a thin ITO antireflection coating, (——) a porous ITO layer, (⋯⋯) an ITO NW layer (all on silicon) and (——) a thin ITO film on glass. Plan view SEM images of each layer are also shown.

In terms of evaluating the improvement afforded by such NW layers as advanced electro-optical device top contacts, the calculated reflectivity at near-normal incidence (10°) as a function of wavelength was determined and is shown in Fig. 1b for the ITO NW layer, a porous ITO layer, a thin ITO film and a standard antireflection layer of ITO on glass. ITO NW layers on silicon exhibited much lower reflectivity than either dense ITO on silicon or porous ITO layers in the wavelength region of interest. Only antireflection ITO coatings on glass showed similar transmission between 850-975 nm, and a usefully low sheet resistivity of ~15 Ω sq^{-1}. Fresnel reflection associated with higher refractive index ITO thin films is virtually eliminated (50) due to reduction in the refractive index from the substrate to the NW layer/ambient interface, where the refractive index was measured to vary from 2.19 (close to the substrate) to 1.04 (at the air interface). The low refractive index NW

layer is optically specular and exhibits a ‘dark’ surface, confirming the absence of Fresnel reflection over a broad spectral width. This is particularly important for LED applications because of the isotropic emission from the active region and the fact that reflection phenomena can limit the light-extraction efficiency.

Typically, ITO and other transparent conducting oxides fail to transmit light in the near infrared region above ~1.1 μm, thus preventing their employment as electrodes for LEDs operating in the second (1.3 μm) and third (1.55 μm) optical communications energy windows. This is due to the onset of a metal-like behaviour at low photon energies, where quanta of incident electromagnetic radiation can couple to plasma oscillations. The surface plasmon resonance (SPR) of ITO (determined using the Drude free-electron model and three-phase Fresnel equations of reflection) is observed at a much lower energy than for metals (where it generally falls into the visible range). In Fig. 1b, the surface plasmon resonance of the ITO NW layer (6895 cm^{-1}) compared to a thin ITO film (10204 cm^{-1}) is red-shifted by ~480 nm, pushing the onset of reflectance further towards the near to mid-IR. The minimum in reflectivity is routinely observed in the crucial 1.2-1.6 μm range at near-normal incidence (0-10°). Angle-resolved reflectance measurements (50) conclusively show that the position of the surface plasmon resonance blue-shifts with increasing angle; the window for maximum transmission over the widest wavelength range is observed near-normal to the surface. Thus, the optical benefits of porosity afforded by the NW growth offsets the standard trade-off between high transparency and low conductivity (and vice versa) by extending conductive transparency into the infra-red, while allowing tunability in the absorption and angle dependent antireflection through structure.

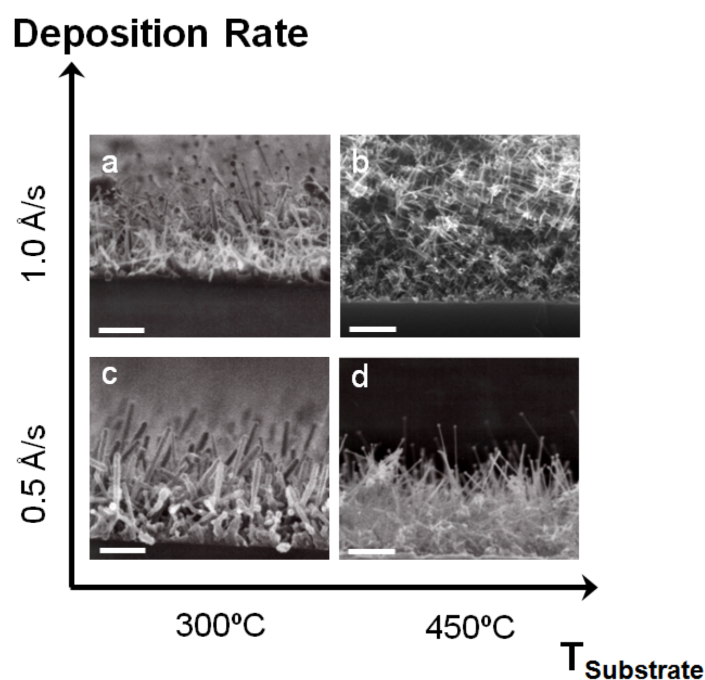

Figure 2. Cross-sectional SEM images of ITO NW layers deposited on silicon as a function of deposition rate and substrate temperature. For all structures, the In:Sn ratio (90:10) was evaporated at a temperature for In and Sn of T_{In} = 835ºC, T_{Sn} = 1000ºC, respectively in an oxygen pressure of 2.1 × 10^{-4} mbar. NWs range between 8-50 nm and are monocrystalline. Scale bars = 200 nm.

The growth rate and temperature are key parameters in the eventual morphology of the ITO NW layers, and these effects on morphology for a defined

composition are summarised in Fig. 2, where consistently finer NWs are found at the higher growth rates and temperatures for a given composition, giving a gamut of similar structures with various porosities that allow tunable absorption or reflection across the visible range.

Indium oxide (In_2O_3) and SnO_2 were also grown as a range of nanodot dispersions. These dispersions have their effective optical constants altered by their effective porosity, characterized by their modal size distributions details of which be found elsewhere (51). An example of In_2O_3 and SnO_2 dispersions are shown in Fig. 3 below alongside ITO nanodots which were possible by halting the intial stages of NW seed formation.

In_2O_3, as a wide bandgap semiconductor ($E_g^d \sim 3.6$ eV; $E_g^i \sim 2.6$ eV), has a transparency that is fundamentally interlinked with it conductivity; the transition occurs on or around its plasma frequency related to the electron density according to the Drude model by $\omega_p^2 = nq^2/m^*\varepsilon_0$, where m^* and q are the effective mass and charge of an electron, and ε_0 the high-frequency permittivity of free-space. For the single-sided In_2O_3 nanodot dispersion, the transmission is limited by Fresnel reflection due to the step discontinuity in refractive index at the rear flat surface (52,53).

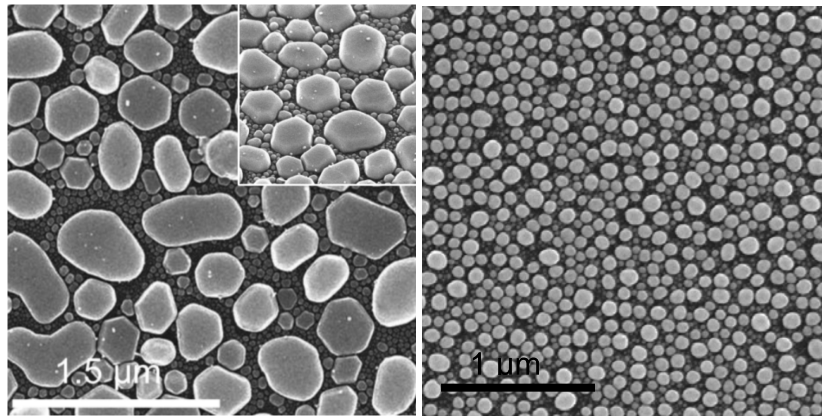

Figure 3. Morphology, distribution and shape differences between In_2O_3 (left) and ITO (right) nanodot dispersions. In_2O_3 are always faceted resulting from post-growth oxidative crystallization of hot substrate dewetted In metal liquid film grown by MBE. The ITO dots form in an oxygen atmosphere from co-deposition of In and Sn.

The In_2O_3 dots, unlike ITO and SnO_2 dots, have large crystals that have a size distribution covering the visible wavelength range, thus causing a transition to Mie scattering which results in the white or grey appearance, rather than a defined colour which varies with angle noted for other dots of smaller sizes and distribution of those sizes. Details on the size and modal distribution can be found elsewhere (51). These layers offer excellent visible to infra-red transmission, and also antireflection properties, as seen in the optical images in Fig. 4a.

Figure 4b shows the integrated total reflectance from a SnO_2 and In_2O_3 nanodots dispersion in the visible and infra-red regions, together with a reference ITO film on glass which exhibits significant increase in transparency as expected in the infra-red. The red-shifting of the entire angle-resolved spectrum for the In_2O_3 nanodot dispersions is also seen in Fig. 4c, where at visible wavelengths the transmission varies from 55% at near incidence, and importantly, remains 87% transparent at wavelengths up to 4 µm compared to the standard transmission of an ITO film on glass.

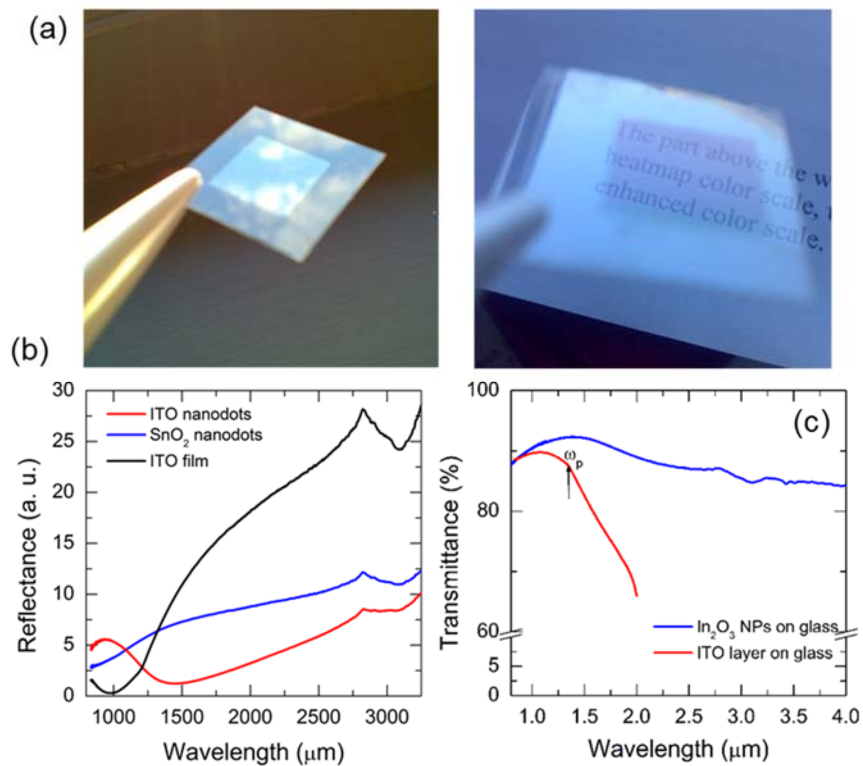

Figure 4. (a) Optical images of the angle-dependent antireflection properties of In_2O_3 nanodot dispersions on a glass cover slip. (b) Integrated total reflectance of ITO, SnO_2 and In_2O_3 nanodot dispersions in the infra-red region and (c) optical transmission characteristics of the In_2O_3 nanodots, all compared to a thin ITO film on glass.

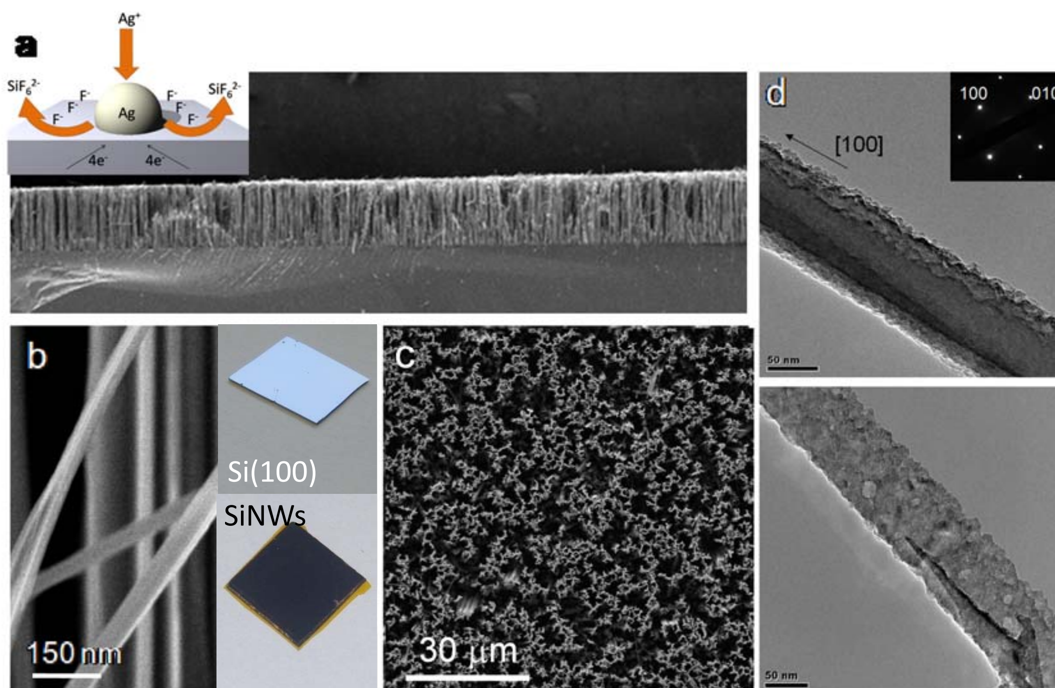

Figure 5. (a) (*Inset*) Schematic of the electroless metal deposition process. Cross-sectional SEM image of the Si NW at low magnification showing the uniformity of the etching depth and NW length. (b) Cross sectional SEM image of several NWs with inset photographs showing pristine Si(100) wafer and wafer with etched NWs. (c) Plan view SEM image of the NW layer. (d) TEM images of individual NWs showing the characteristic rough morphology of MAC etched NWs.

Silicon NW layers that offer good broadband absorption, and a near blackbody response at certain angles to white light, are possible by electrolessly etching single crystal silicon until a disordered array of rough NWs with a wide diameter distribution are formed. Figure 5 shows the resulting SiNW layers that are formed using the metal-assisted chemical (MAC) etching approach described above, and summarized schematically in Fig. 5a. Vertical arrays of NWs are formed across the entire surface of the wafer, as shown in the cross-sectional SEM image in Fig. 5a. High resolution SEM examination reveals that the NWs have an average length of 115 μm. Examination of the top surface of the Si NW layers shows that the wires appear in non-uniform distributions characterized by clumped regions of high density NWs and correspondingly, regions of locally less density (Fig. 5c). Further examination shows that the less dense regions are not devoid of NWs, rather the NWs are bent towards each other forming the high density regions. This stems from a combination of high length-to-width aspect ratio and capillary forces related to the post-etch cleaning procedure. NWs were measured to have an average width of 80 nm, shown in Fig. 5b. TEM analysis in Fig. 5d also confirmed that individual Si NWs are single crystal and electron diffraction measurements also confirm their (100) orientation, consistent with etching from bulk Si(100). The NWs have a characteristic rough morphology consistent with MAC etched NWs in previous reports. Figure 5b shows typical SEM and optical images (inset) of the pre and post-etched Si, where at angles between 45 and 55°, a completely black, strongly absorbing layer is visible. Such layers are being sought for silicon based photovoltaics, and their broadband absorption characteristics are typical of marginally controlled etching characteristics (facilitated by the reduction potential of Ag ions in HF solutions), giving a highly disorder array on several lengths scales (porosity of the semiconductor crystal, roughness on the walls of the wires, bent and clumped NWs randomly distributed throughout the vertical array etc., that facilitate a very high degree of optical scattering effects.

<u>Bottom-up growth of fully transparent contact layers of indium tin oxide NWs for LEDs</u>

One particular application of ITO that employs its conductive and transmissive properties, is that of an ohmic contact for LEDs, but has until now, only had limited success due to high resistivities and an unacceptable trade-off between its electrical and optical characteristics. The limited availability of materials with desired refractive indices, however, has prevented the implementation of optical components with very high performance. The possibility of forming controlled complex, multi-level branched structures with optimized optical properties in a single-step, bottom-up growth regime, is a real advance considering their compatibility with optoelectronic device architectures.

We have developed a controllable molecular beam epitaxial growth system for obtaining high quality, uniphasic, branched ITO NWs on silicon and oxidised silicon surfaces using In and Sn precursors in an oxygen atmosphere. The NW layer morphology and transparency can be tailored through rational control of the evaporation-condensation parameters, and will be shown to result in bottom-up grown layers of self-catalysed and seeded NWs with excellent electrical, optical and homogeneous structural properties, that can even be grown as large area (several cm^2) contacts. The graded porosity NW layers are grown as an alternative option for the standard NiCr top contact on a Si/SiGe multi-quantum well (MQW) LED, exhibiting a transparency of >80 % in the visible and >90% in the 1.2–1.6 μm range.

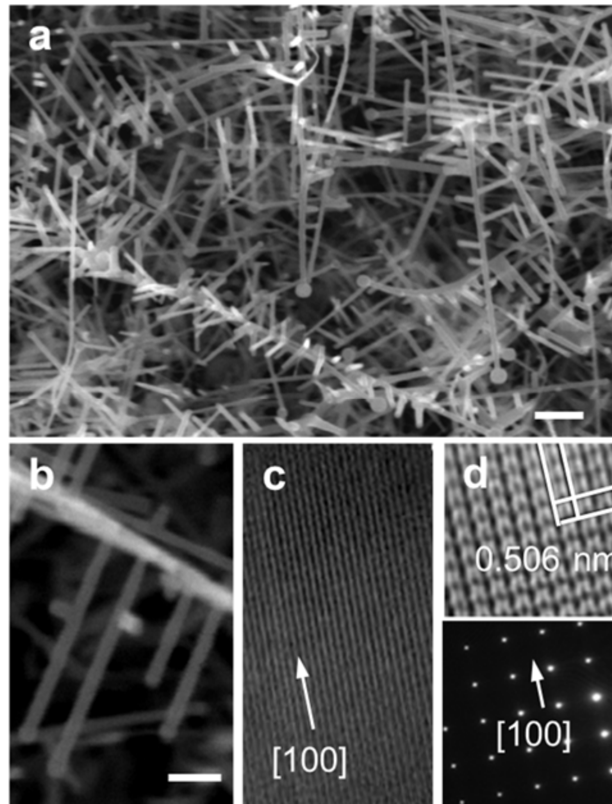

Figure 6. (a) FESEM image of the interior of a typical ITO NW array grown at T_{sub} = 500 °C at nominal In:Sn (90:10) growth rates of 0.1 nm s^{-1} highlighting the mutually orthogonal [100] branching from the principal ITO NW backbone in three dimensions. Scale bar = 50 nm. (b) Higher magnification images of homogenous branching events. The scale bars = 25 nm. (c) HRTEM image of an individual NW highlighting interplanar spacings and the [100] growth direction. (d) The higher magnification HRTEM image and associated SAED pattern identify monocrystalline $(In_{1.875}Sn_{0.125})O_3$ with (002) and (020) interplanar spacings of 0.506 nm.

Various morphologies for graded refractive index coatings are possible by choosing any of the NW morphologies or nanodot dispersions according to deposition rate and substrate temperatures. For NWs, a distinct growth mode modification from compact (but rough and partially porous) layers to dendritic NW growth during deposition is achievable at specific growth rates and substrate temperatures. Locally increased porosity is the main defect found in graded index porous layer growth by oblique angle deposition techniques; such problems are not encountered for dense, highly branched NW layers as outlined below in Fig. 6. No heterogeneous catalysts are required and we still observe extremely high quality, defect-free NWs comprising the layers.

After the growth was optimized on both quartz and silicon substrates, the growth method was applied to corresponding n–i–p^+ Si/SiGe MQW device structures, which in the device employed in this work consisted of an active region with a 15 period $Si/Si_{0.77}Ge_{0.23}/Si$ MQW layer. An example of an ITO NW layer grown on the Si/SiGe MQW structure is shown in the SEM image in Fig. 7a with a corresponding device schematic shown in Fig. 7b.

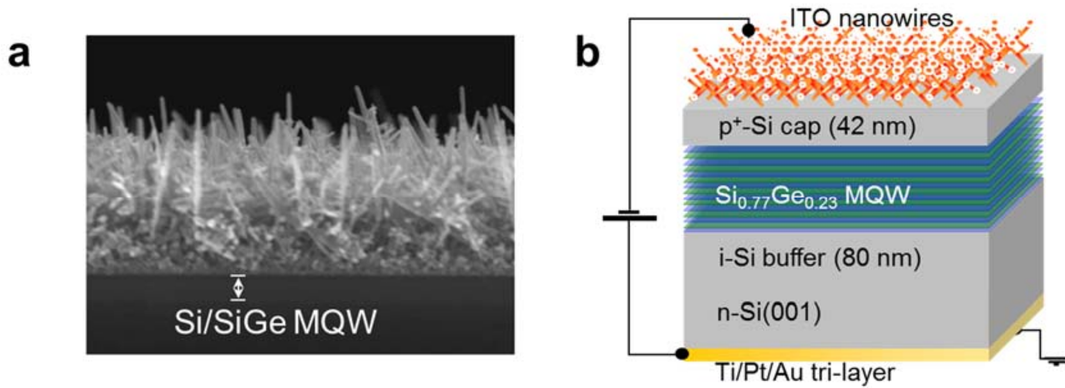

Figure 7. (a) Cross-sectional SEM images of the NW layer on a SiGe MQW. The NW layer shown was grown at a substrate temperature of T_{sub} = 575 ºC at a growth rate of 0.2 nm s^{-1} and an invariant oxygen partial pressure of 2.1 × 10^{-4} mbar. (b) Schematic representation of the ITO NW contacted SiGe MWQ LED. The active region consists of a 15 period $Si/Si_{0.77}Ge_{0.23}/Si$ multiple quantum well layer. The bottom contact is a Ti/Pt/Au trilayer. The NWs were grown directly onto the p^+-Si.

To assess this influence on the optical transmission, ITO layers of varied thickness and morphology were grown on quartz substrates. Figure 8a shows their transmission spectra in the wavelength range 400-1600 nm. The inset shows a typical ITO NW layer deposited on a glass cover slip. The transparency in the visible range improves to ~90% with increasing growth rate up to 0.2 nm s^{-1}. Spectroscopic ellipsometric measurements show effective refractive indices of the NW layer-air interface to be between 1.04–1.12 for all samples investigated, directly due to the varied porosity of the nanostructured layers, calculated using the Bruggemann effective medium approximation. This is very advantageous as previous efforts to couple high transmission and low resistivity resorted to ITO/Ag/ITO multilayer sandwiches to combine the improved conductivity of Ag and the high refractive index of the ITO (η = 2.19) to boost transmittance of the metal interlayer (54,55). The measured absorption edge for the nanostructured ITO films is ~380 nm, a value lower than that for ITO on glass and comparable to ITO/YSZ lattice matched thin films and NWs (56).

Their suitability to silicon-based LEDs, is demonstrated by investigation of the room temperature electroluminescence (EL) emission from the NW contacted SiGe MQW LED, shown in Fig. 8a, showing unambiguously that the Si and SiGe emission lines are fully resolved through the NW layer contact in ambient laboratory conditions. The corresponding comparative spectra of both the uncoated MQW and nanostructured ITO-contacted MQW are shown in Fig. 9a, where a marked improvement in transmission compared to the NiCr contacted MQW is observed for electroluminescence emission. The highest attenuation was noted for the Si^{EHD} emission, although 20% of the uncoated MQW signal for this line was still transmitted, as opposed to negligible transmission through the NiCr contact. The Si_{BE}^{TO} emission was attenuated by ~50% but of utmost interest are the SiGe emission lines, which were transmitted with negligible absorption. It is clear that the full spectrum (all important transitions) of a SiGe MQW LED can be resolved through the ITO NW top contact.

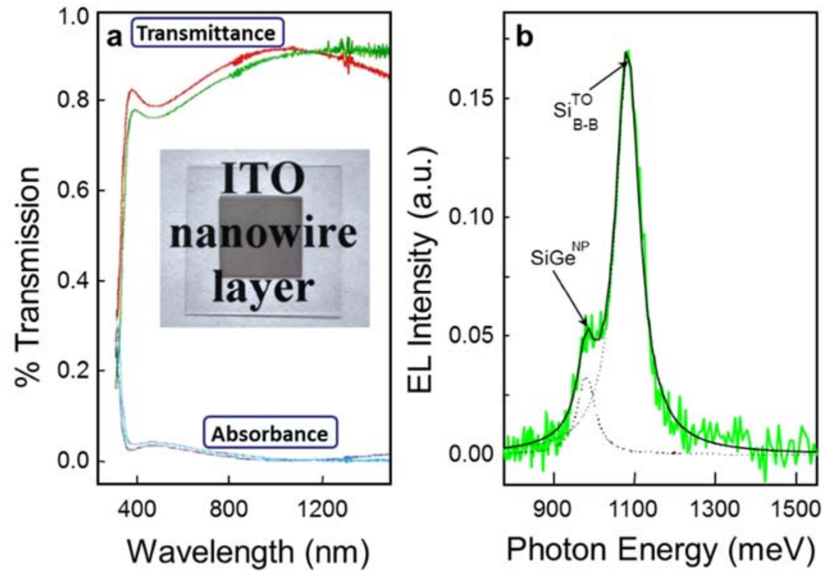

Figure 8. (a) Transmission measurements of an ITO NW layer deposited at a substrate temperatures of T_{sub} = 575 ºC (——) and T_{sub} = 450 ºC (——) at a nominal growth rate of 0.05 nm s^{-1} and an invariant oxygen partial pressure of 2.1 × 10^{-4} mbar. The inset shows an ITO NW layer deposited on a glass cover slip. (b) Room temperature (295 K) electroluminescence (EL) spectrum from an ITO NW-contacted Si/SiGe MQW structure acquired at an injection current of 575 mA. The $SiGe^{NP}$ (no phonon) and $Si^{TO}{}_{B\text{-}B}$ (band-to-band transverse optical phonon) emission were extracted with a multiple Gaussian fit.

The geometry of the NW layer maximizes transmission through a single-step, practical approach of randomizing scattering photons. In addition, the emission is maximised by the angular dependence of the plasma frequency, where the transmission is both maximized and limited to near-normal output. The optical and electrical properties as a whole are unprecedented for any conductive, transparent oxide and have the added benefit of being experimentally much simpler than more complex, multi-step deposition of several defect-free layers of reducing refractive index (exhibiting poor conductivities) and highly conducting thin films (exhibiting poor transmission in the visible region).

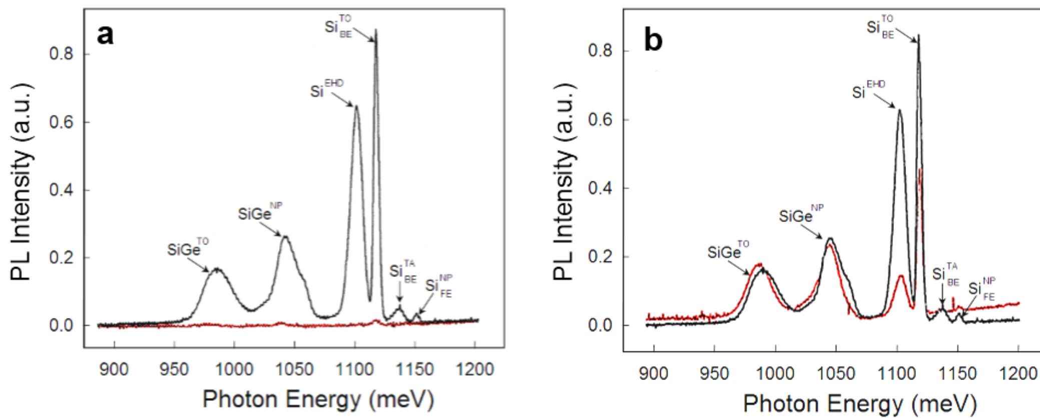

Figure 9. Comparison of the low temperature (45 K) photoluminescence spectra of (a) a non-contacted SiGe MQW (——) and a NiCr contacted SiGe MQW (——) (b) a non-contacted SiGe MQW (——) and an ITO NW-contacted SiGe MQW (——). The two high intensity peaks observed at 1125 and 1150 nm correspond to the silicon transverse optical phonon-assisted bound exciton recombination ($Si_{BE}{}^{TO}$) and the silicon electron-hole droplet emission (Si^{EHD}), respectively.

Phonon engineering in Si nanostructures for thermoelectrics

It has been shown that when crystalline solids are confined to the nanometer range, electron and phonon transport can be significantly altered due to three discrete effects (57) such as increased boundary scattering, changes in phonon dispersion, and quantization of phonon transport. Similarly, theoretical and experimental work (58) has shown that the electrical and thermal conductivities from NWs differ from those for bulk Si (59). Furthermore, transport properties are very sensitive to the crystalline lattice characteristics of individual NWs. Consequently, systematic structural characterization is necessary to distinguish these characteristics.

Silicon has not been considered a viable thermoelectric energy converter due to its exceptionally high thermal conductivity. Heat carried by phonons in Si have large mean-free-path lengths >200-300 nm (60). Reducing the dimensionality of all or part of a crystal has been shown to be an effective method for increasing thermal resistivity (61-65). For Si at room temperature, useful thermoelectric figures of merit need a lattice thermal conductivity of ~1W/m-K. Thermal conduction limited by grain boundary scattering processes predict that small feature sizes (~2 nm) can make Si a viable thermoelectric (66,67), and methods to engineer such sizes are a focus of research interest.

Using MAC etched Si NWs described in Fig. 5, nanostructuring of Si NWs on more than one length scale allows for a significant increase in thermal resistance, beyond Umklapp process and boundary scattering. By etching Si with a defined resistivity, the resulting NWs can exhibit a high degree of roughness defined by small crystallites of silicon that are not simple edges of rough features delineated by the anisotropic electroless etching process (68-70). Lightly doped p-type Si results in rough NWs coated with a high density of crystallites that are oriented in a range of zone axes different to that of the NW itself, as shown in the bright field and high angle annular dark field image of a rough Si NW in Fig. 10a and b. These structures are effective phonon confining crystallites that also increase the boundary scattering for phonons, thereby increasing the thermal resistance.

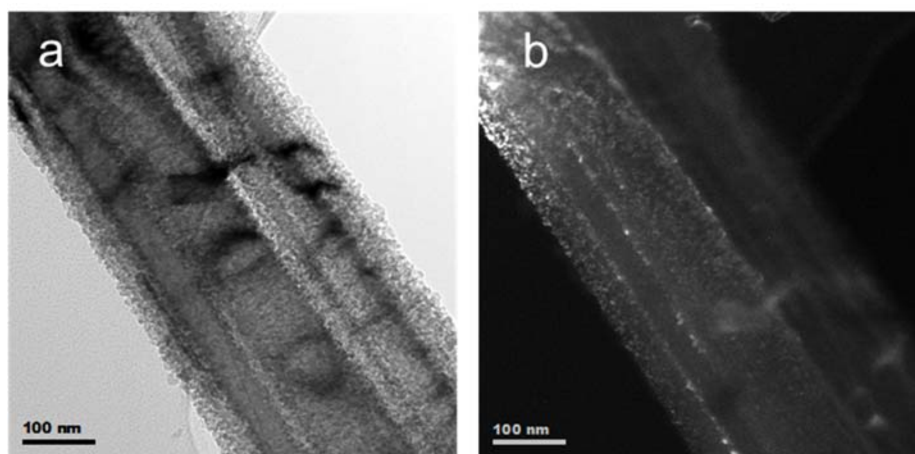

Figure 10. (a) Bright field and (b) high angle annular dark field TEM image of a rough p-type Si NW.

For horizontally oriented Si NWs, a deconvoluted contribution to the asymmetry in the TO phonon peak is found at 506 cm^{-1} (Figure 11a). This deconvoluted band at 506 cm^{-1} is not expected for nanosized diamond cubic Si. It has been shown that this band is due to the presence of hexagonal Si structure. This agrees well with the Raman measurements made on hexagonal diamond Si obtained by

nanoindentation (71). The results are also comparable to the measurements realized in microcrystalline samples with a mixture of cubic and hexagonal diamond Si phases in agreement with semi empirical models. In our case, contributions at these frequencies due to oxide presence cannot explain the observation of the convoluted band at elevated temperature, despite evidence that a non-uniform oxide is present along the length of all wires investigated.

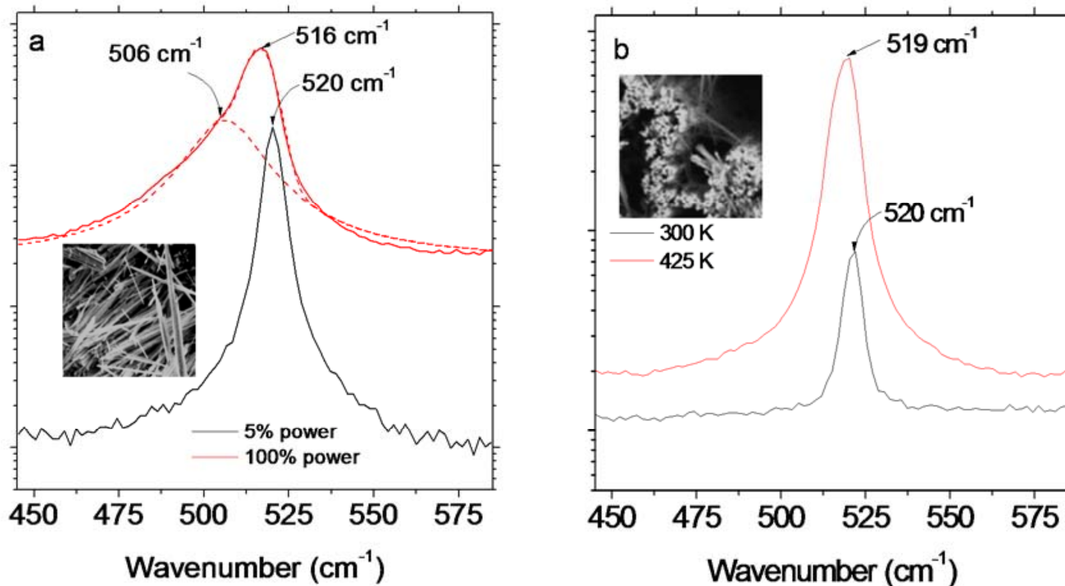

Figure 11. (a) Raman scattering of the TO phonon from (a) v-SiNWs and (b) h-SiNWs as a function of temperature. Spectra were acquired at 5, 10 and 100% of incident laser power.

In Fig. 12, the TO mode is shown for four of the spectra, as marked in Fig. 12a. We observe the characteristic small redshift from 521 to ~519 cm^{-1} which reverts to 521 cm^{-1} when the spectrum is again taken from the vertically oriented Si NWs. This confirms the contribution from confining crystallites along the outer surface of the NWs; their contribution is seen when their inelastic scattering cross section is increased during probing of the sides of the NWs.

Future work is ongoing to define the thermal resistance changes in Si NWs with increased surface roughness that enhances the red-shifting and asymmetric broadening of their Raman spectra. SiO_x contributions were not evident and specific substrate Raman modes were suppressed for horizontal NWs. The correlation length *L* estimated by this model is related to the average grain size in nanocrystalline materials or to the average distance between defects in crystals but alone does not give a satisfactory description of the Raman band-shape modification for the data. However, the ability to strongly affect phonon transport results in inelastic scattering characteristics that are directly related to a significant lowering of the thermal conductance augers well for optimization of simple and quick electrochemical processes for engineering of phonon transport in Si nanostructures for thermoelectrics.

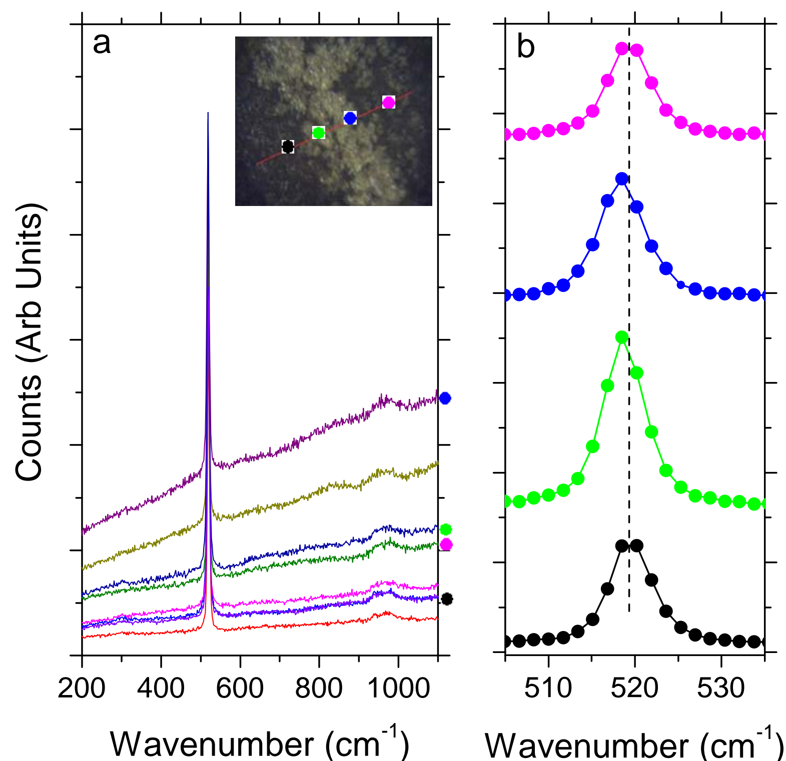

Figure 12. (a) Raman scattering spectra acquired by crossing from regions of v-SiNWs to h-SiNWs and then to v-SiNWs. (*Inset*) Optical image taken from the spectrometer showing the h-SiNWs (light region) and vertical NWs (dark flanking regions) and points of Raman measurements. (b) Variation in TO phonon scattering frequency as a function of position shown in the optical image in (a).

Si, In_2O_3 and SnO_2 nanostructures as anode materials for Li-ion batteries

To increase the energy content of lithium-ion batteries, significant research has been devoted to finding higher capacity electrode materials. On the cathode side, sulphur and oxygen-based positive electrodes have recently been intensely researched (72-74). On the anode side, alloy anodes have shown significant promise. An ideal anode material should possess high gravimetric and volumetric capacity, a low potential against cathode materials, long cycle life, light weight, environmental compatibility, low toxicity, and low cost (75). Silicon has performance that make it a very attractive choice as an anode material, given its ability to mitigate volumetric expansion pulverization that can result in electrical disconnect and disintegration during operation over many cycles, and the fact that it has the highest theoretical specific capacity for Li^+ intercalation.

We have studied Si NW layers by comparison to associated bulk Si(100) samples to deduce the direct effect of nanostructuring on identically doped Si where all NWs formally have the same crystal orientation. In addition, the ability of porous and graded index transparent conducting oxides such as In_2O_3 and SnO_2 similar to those shown in Fig. 3, which are excellent alloy materials, represent some of the most promising anode reactions for safe high capacity Li-ion batteries. These dispersions also allow for the possibility of optical probing of intercalation and related electrochemical processes. Both transparent oxide materials allow rechargeable alloying with Li, resulting in stable and efficient reversible charge storage. For both

materials, the dispersion of sizes is critical in their evaluation and analysis towards future development.

Figure 13 shows the first five voltammetric cycles of an SnO_2 nanodot electrode, and we note that the reduction of SnO_2 to Sn^0, allows an alloy reaction with Li. The cyclic voltammograms of SnO_2 show that the cathodic process involved the insertion of Li into Sn_2O_3 to form a Li–Sn alloy (charging) and the anodic process follows Li extraction or dealloying (discharging). Details of the In_2O_3 electrode can be found elsewhere (76). The first cycle for each of the dispersions confirms SEI layer formation at the higher cathodic potentials. For both materials, the Li insertion potentials remain quite low. A related process is known to occur for Li alloying with Sn (77).

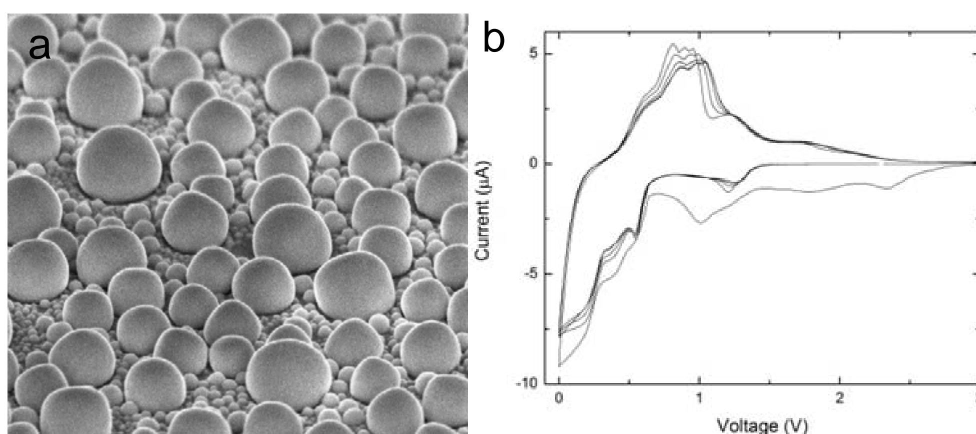

Figure 13. SEM image of epitaxial non-faceted SnO_2 nanodots on Si(100) with corresponding cyclic voltammograms.

Here, the dispersion of the nanodots, while permitting transparency and conductivity into the IR region, also allows lithium insertion into the current collector, and remains structurally stable due to strong epitaxial adhesion and lithium co-insertion buffering by the silicon current collector. The partial porosity of the variable size nanodot distribution prevents stress build-up in the In^0 and Sn^0 (when reduced from In_2O_3 and SnO_2) and promotes optical transparency. The removal of the smallest nanodots by volume expansion of the underlying silicon does not greatly affect the gravimetric energy density, and it serves to buffer polarization of the Li_xIn and Li_xSn by reversibly inserting Li^+.

Si NWs also offer the possibility of reversible Li insertion, even when etched from Si wafers. Figure 14 shows cyclic voltammograms of a Si(100) electrode and a Si NW electrode etched from the same structure, also shown in Fig. 14. Si NWs on a silicon current collector exhibit reversible lithium insertion potentials, identical to those from the bulk Si(100) substrate. The Si(100) undergoes some surface morphological changes, where cracking of the surface occurs, freeing up fresh Si for intercalation, resulting in self-similar cyclic voltammetric response with a good coulometric efficiency. For lower doped Si(100), however, we note that cracking is much less evident, due to a reduced Li^+ uptake by a lower carrier (electron) density in the p-type materials compared to n-type. For the NWs, considerable space charge capacitance contributed to the measured charge, and further work is underway to define the transition from intercalation to pseudocapacitance for these materials.

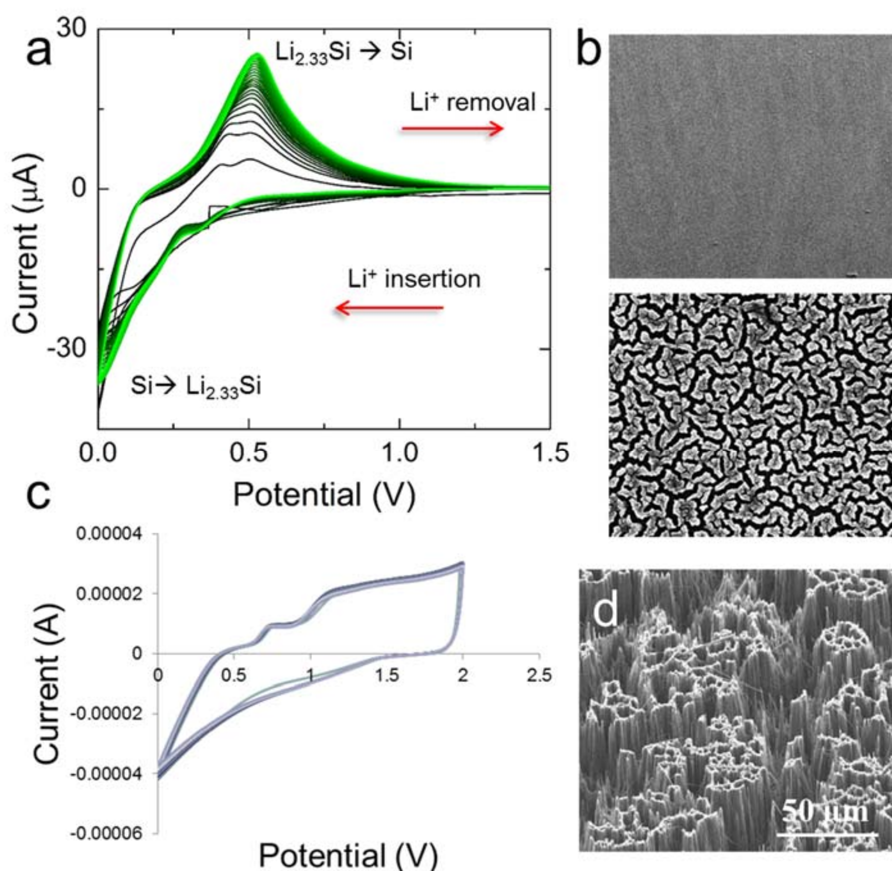

Figure 14. (a) Cyclic voltammograms of p-type Si(100) in a 1 mol dm^{-3} electrolyte containing $LiPF_6$ in EC:DMC (50:50 v/v) at a scan rate of 1 mV s^{-1}. (b) SEM image of the p-type (top) and n-type (bottom) surfaces following 30 potentiodynamic cycles. (c) Cyclic voltammograms of the p-type Si NWs, and (d) SEM image of the p-type Si NWs.

Conclusions

The fabrication of high aspect ratio monocrystalline and highly transparent doped metal-oxide NW layers and electroless etching of silicon into vertical NW layers with unprecedented simplicity in morphological control and phase homogeneity was presented. The NWs prove to be excellent materials for broadband absorption, tunable reflection characteristics useful for optoelectronic and related devices, but also have useful structural and electrochemical properties that allow reversible charge storage as Li-ion battery anodes. The roughness of Si NWs also has a marked effect on phonon transport, allowing for lower thermal conductance and the possibility for junctionless power from temperature differences. Structuring semiconductors through top down electrochemical means or through grading porosity through bottom up growth methods, allows for a variety of useful electrochemical electrical, optical and structural effects that are amenable for further consideration in energy related materials research.

Acknowledgements

This work was supported by Science Foundation Ireland (SFI) under contract No. 07/SK/B1232a. CG, MO and EA acknowledge financial support from the Irish Research council under Awards No. RS/2011/797, RS/2010/2170, and RS/2010/2920. EA acknowledges SFI for a Short Term Travel Fellowship under award No.

07/SK/B1232a-STTF11. Part of this work was conducted under the framework of the INSPIRE programme, funded by the Irish Government's Programme for Research in Third Level Institutions, Cycle 4, National Development Plan 2007-2013. The authors also acknowledge financial support from the European Union 7th Framework Programme under the SiNAPS project (project ref: 257856).

References

[1] H. Föll, S. Langa, J. Carstensen, M. Christophersen and I.M. Tiginyanu, *Adv. Mater.* **15**, 183 (2003).

[2] E. Spiecker, M. Rudel, W. Jäger, M. Leisner and H. Föll, *phys. stat. sol. (a)* **202,** 2950 (2005).

[3] S. Langa, J. Carstensen, I.M. Tiginyanu, M. Christophersen and H. Föll. *Electrochem. Solid-State Lett.* **5**, C14 (2002).

[4] M. Christophersen, S. Langa, J. Carstensen, I.M. Tiginyanu and H. Föll, *phys. stat. sol. (a)* **197**, 197 (2003).

[5] S. Lölkes, M. Christophersen, S. Langa, J. Carstensen and H. Föll, *Mater. Sci. Eng. B*, **101**, 159 (2003).

[6] S. Langa, J. Carstensen, M. Christophersen, K. Steen, S. Frey, I.M. Tiginyanu and H. Föll, *J. Electrochem. Soc.* **152**, C525 (2005).

[7] F.M. Ross, G. Oskam, P.C. Searson, J.M. Macaulay and J.A. Liddle, *Philos. Mag. A* **75**, 525 (1997).

[8] H. Tsuchiya, M. Hueppe, T. Djenizian and P. Schmuki, *Surf. Sci.* **547,** 268 (2003)

[9] H. Tsuchiya, M. Hueppe, T. Djenizian, P. Schmuki and S. Fujimoto, *Sci. Tech. Adv. Mater.* **5**, 119 (2004).

[10] S. Langa, I.M. Tiginyanu, J. Carstensen, M. Christophersen and H. Föll, *Appl. Phys. Lett.* **82**, 278 (2003).

[11] S. Langa, M. Christophersen, J. Carstensen, I.M. Tiginyanu and H. Föll, *phys. stat. sol. (a)* **197**, 77 (2003).

[12] A.-M. Gonçalves, L. Santinacci, A. Eb, C. David, C. Mathieu, M. Herlem and A. Etcheberry, *phys. stat. sol. (a)* **204**, 1286 (2007).

[13] A.-M. Gonçalves, L. Santinacci, A. Eb, I. Gerard, C. Mathieu and A. Etcheberry, *Electrochem. Solid-State Lett.* **10**, D35 (2007).

[14] M.M. Faktor, D.G. Fiddyment and M.R. Taylor, *J. Electrochem. Soc.,* **122**, 1566 (1975).

[15] E. Harvey, C. Heffernan, and D. N. Buckley and C. O'Raifeartaigh, *Appl. Phys Lett.*, **81**, 3191 (2002).

[16] L. Macht, J.J. Kelly, J.L. Weyher, A. Grzegorczyk and P.K. Larsen, *J. Crystal Growth* **273**, 347 (2005).

[17] J. J. Kelly, L. Macht, D.H. van Dorp, M.R. Kooijman and J.L, Weyher, *in Processes at the Compound-Semiconductor/Solution Interface*, Editors: P.C. Chang, K. Shiojima, R.E. Kopf, X. Chen, D. Noel Buckley, A. Etcheberry, and B. Marsan, State-of-the-Art Program on Compound Semiconductors XLII, **PV 2005-04**, p. 138 (2005).

[18] R. Lynch, C. O'Dwyer, D.N. Buckley, D. Sutton and S.B. Newcomb, *ECS Trans* **2**, 131 (2006).

[19] R. Lynch, M. Dornhege, P. Sánchez Bodega, H.H. Rotermund and D.N. Buckley, *ECS Trans* **6,** 331 (2007).

[20] R. Lynch, C. O'Dwyer, D. Sutton, S. Newcomb, and D.N. Buckley, *ECS Trans* **6,** 355 (2007).

[21] R. Lynch, C. O'Dwyer, N. Quill, S. Nakahara, S.B. Newcomb, and D.N. Buckley, *ECS Trans* **16**, 393 (2008).

[22] N. Quill, C. O'Dwyer, R. Lynch, C. Heffernan, and D. N. Buckley, *ECS Trans* **19**, 295 (2009).
[23] C. O'Dwyer, D.N. Buckley, D. Sutton, and S.B. Newcomb, *J. Electrochem. Soc.,* **153,** G1039 (2006).
[24] C. O'Dwyer, D.N. Buckley, and S. B. Newcomb, *Langmuir*, **21**, 8090 (2005)
[25] C. O'Dwyer, D.N. Buckley, D. Sutton, M. Serantoni, and S.B. Newcomb, *J. Electrochem. Soc.,* **154**, H78 (2007).
[26] O. V. Bilousov, J. J. Carvajal, D. Drouin, X. Mateos, F. Díaz, M. Aguiló and C. O'Dwyer, *ACS Appl. Mater. Interfaces*, **4**, 6927 (2012).
[27] C. K. Chan, H. L. Peng, G. Liu, K. McIlwrath, X. F. Zhang, R. A. Huggins, Y. Cui, *Nat. Nanotechnol.* **3** (2008) 31 (2008).
[28] M. T. McDowell, S.W. Lee, C. Wang, Y. Cui, *Nano Energy* **1**, 401 (2012)
[29] M. T. McDowell, Y. Cui, *Adv. Energy Mater.* **1,** 894 (2011).
[30] J. Y. Tang, H. T. Wang, D. H. Lee, M. Fardy, Z. Y. Huo, T. P. Russell, and P. D. Yang, *Nano Lett.* **10**, 4279 (2010).
[31] H. S. Yang, D. G. Cahill, X. Liu, J. L. Feldman, R. S. Crandall, B. A. Sperling, and J. R. Abelson, *Phys. Rev. B* **81**, 104203 (2010).
[32] A. I. Hochbaum, R. K. Chen, R. D. Delgado, W. J. Liang, E. C. Garnett, M. Najarian, A. Majumdar, and P. D. Yang, *Nature* **451**, 163 (2008).
[33] D. S. Ginely, C. Bright, *MRS Bull.* **25**, 15 (2000).
[34] Y. Cui, C. M. Lieber, *Science* **291**, 851 (2006).
[35] Y.-J. Hsu, S.-Y. Lu, J. *Phys. Chem. B* **109**, 4398 (2005).
[36] J. G. Lu, P. Chang, Z. Fan, *Mater. Sci. Eng. R* **52**, 49 (2006).
[37] M. C. Johnson, S. Aloni, D. E. McCready, E. Bourret-Courchesne, *Cryst. Growth Des.* **6**, 1936 (2006).
[38] P. Nguyen, et al. *Nano Lett.* **3**, 925 (2003).
[39] Q. Wan, et al. *Nano Lett.* **6**, 2909 (2006).
[40] D.-W. Kim, et al. *Nano Lett.* **7**, 3041 (2007).
[41] D. L. Wang, C. M. Lieber, *Nature Mater.* **2**, 355 (2003).
[42] J.M. Tarascon, M. Armand, *Nature* **414**, 359 (2001).
[43] M.S. Whittingham, *Chem. Rev.* **104**, 4271 (2004).
[44] M. Armand, J.M. Tarascon, *Nature* **451**, 652 (2008).
[45] D. Linden, T. Reddy, Handbook of Batteries, McGraw-Hill, New York, 2002.
[46] J. B. Goodenough, H. Abruna, M. Buchanan, US Department of Energy, Washington, DC, 2007.
[47] C. Liu, F. Li, L.P. Ma, H.M. Cheng, *Adv. Mater.* **22**, E28 (2010).
[48] Y. J. Lee, H. Yi, W.J. Kim, K. Kang, D. S. Yun, M. S. Strano, G. Ceder, A. M. Belcher, *Science* **324**, 1051 (2009).
[49] B. Scrosati, J. Garche, J. *Power Sources* **195**, 2419 (2010).
[50] C. O'Dwyer, M. Szachowicz, G. V. Visimberga, V. Lavayen, S. B. Newcomb, C. M. Sotomayor Torres, *Nat. Nanotech.* **4**, 239 (2009).
[51] M. Osiak, W. Khunsin, E. Armstrong, T. Kennedy, C. M. Sotomayor Torres, K. M. Ryan, and C. O'Dwyer, *Nanotechnology*, **24**, 065401 (2013).
[52] J. Q. Xi, J. K. Kim and E. F. Schubert, *Nano Lett.* **5**, 1385 (2005).
[53] J.-Q. Xi, M. F. Shubert, J. K. Kim, E. F. Shubert, M. Chen, S.-Y. Lin, W. Liu and J. A. Smart, *Nature Photon.* **1**, 176 (2007).
[54] C. G. Granqvist, A. Hultåker, *Thin Solid Films* **411**, 1 (2002)
[55] S. Ju, *et al. Nat. Nanotech.* **2**, 378 (2007).
[56] Q. Wan, P. Feng, T. H. Wang, *Appl. Phys. Lett.* **89**, 123102 (2006).
[57] M. S. Dresselhaus, G. Dresselhaus, and A. Jorio, *Annu. Rev. Mater. Res.*, **34**, 247 (2004).
[58] D. Li, Y.Wu, P. Kim, L. Shi, P. Yang, and A. Majumdar, *Appl. Phys. Lett.* **83**, 2934 (2003).

[59] A. I. Hochbaum, D. Gargas, Y. J. Hwang, and P. Yang, *Nano Lett.,* **9**, 3350 (2009).
[60] K. Esfarjani, G. Chen, and H. T. Stokes, *Phys. Rev. B* **84**, 085204 (2011).
[61] L. Weber and E. Gmelin, *Appl. Phys. A* **53**, 136 (1991).
[62] D. Y. Li, Y. Y. Wu, P. Kim, L. Shi, P. D. Yang, and A. Majumdar, *Appl. Phys. Lett.* **83**, 2934 (2003).
[63] Y. S. Ju and K. E. Goodson, *Appl. Phys. Lett.* **74**, 3005 (1999).
[64] W. J. Liu and M. Asheghi, ASME Trans. *J. Heat Transfe*r **128**, 75 (2006).
[65] P. E. Hopkins, C. M. Reinke, M. F. Su, R. H. Olsson, E. A. Shaner, Z. C. Leseman, J. R. Serrano, L. M. Phinney, and I. El-Kady, *Nano Lett.* **11**, 107 (2010).
[66] A. K. McCurdy, H. J. Maris, and C. Elbaum, *Phys. Rev. B* **2**, 4077 (1970).
[67] H. B. G. Casimir, *Physica* **5**, 495 (1938).
[68] O. Lotty, N. Petkov, Y. M. Georgiev and J. D. Holmes, *Jpn. J. Appl. Phys.* **51**, 11PE03 (2012).
[69] W. McSweeney, O. Lotty, J. D. Holmes, C. O'Dwyer, *ECS Trans.* **35**, 25 (2011).
[70] C. Glynn, O. Lotty, W. McSweeney, J. D. Holmes, C. O'Dwyer, *ECS Trans.* **8**, 73 (2011).
[71] A. Fontcuberta i Morral, J. Arbiol, J. D. Prades, A. Cirera, and J. R. Morante, *Adv. Mater.* **19**, 1347 (2007).
[72] Y. Yang, M.T. McDowell, A. Jackson, J.J. Cha, S.S. Hong, Y. Cui, *Nano Lett.* **10**, 1486 (2010).
[73] B. L. Ellis, K. T. Lee, L. F. Nazar, *Chem. Mater.* **22**, 691 (2010).
[74] X. L. Ji, K. T. Lee, L. F. Nazar, *Nat. Mater.* **8**, 500 (2009).
[75] J. R. Szczech, S. Jin, *Energy Environ. Sci*. **4**, 56 (2001).
[76] M. Osiak, W. Khunsin, E. Armstrong, T. Kennedy, C. M. Sotomayor Torres, K. M. Ryan, and C. O'Dwyer, *ECS Trans.* (*ibid.*) (2013).
[77] J. S. Chen, X. W. Lou, *Mater. Today* **15**, 246 (2012).